Research Paper

Soft-template synthesis of mesoporous non-precious metal catalyst with Fe-N_x/C active sites for oxygen reduction reaction in fuel cells

Yeongdong Mun[a,1], Min Jeong Kim[b,1], Shin-Ae Park[c], Eunsung Lee[d], Youngjin Ye[a], Seonggyu Lee[a], Yong-Tae Kim[c], Sungjun Kim[b], Ok-Hee Kim[e], Yong-Hun Cho[f], Yung-Eun Sung[b,**], Jinwoo Lee[a,*]

[a] Department of Chemical Engineering, Pohang University of Science and Technology (POSTECH), 77 Cheongam-Ro, Nam-gu, Pohang 790-784, Gyeongbuk, Republic of Korea
[b] Center for Nanoparticle Research, Institute for Basic Science (IBS)/School of Chemical and Biological Engineering, Seoul National University (SNU), Seoul 08826, Republic of Korea
[c] Department of Energy System, Pusan National University, Busan 609-735, Republic of Korea
[d] Department of Chemistry, Pohang University of Science and Technology (POSTECH), 77 Cheongam-ro, Nam-gu, Pohang 790-784, Gyeongbuk, Republic of Korea
[e] Department of Science, Republic of Korea Naval Academy, Jinhae-gu, Changwon 646-797, Republic of Korea
[f] Department of Chemical Engineering, Kangwon National University, Samcheok 245-711, Republic of Korea

ARTICLE INFO

ABSTRACT

We synthesized ordered mesoporous Fe/N/C with highly active Fe-N_x/C sites denoted as m-FePhen-C as a non-precious metal catalyst (NPMC) for the oxygen reduction reaction in fuel cells. This was the first study that incorporated a catalyst precursor with Fe-N coordination directly in a simple block co-polymer-assisted soft-template method for the synthesis of mesoporous Fe/N/C. The synthesized catalyst (m-FePhen-C) showed a high catalytic performance comparable to that of Pt/C in half-cell tests, and a membrane electrode assembly (MEA) with an m-FePhen-C cathode exhibited 40% higher power density than did an MEA with a commercial Pt/C cathode in single-cell tests, with comparable electrode thicknesses. This result is highly meaningful in that generation of the Fe-N_x/C active sites and formation of ordered mesoporous structure were achieved simultaneously in the simple soft-template-assisted process, and in that the advantages of mesoporous structure with appropriate pore size in metal-containing NPMC were elucidated for high-performance MEAs.

1. Introduction

A fuel cell that uses a polymer electrolyte and operates at low temperature is a promising substitute for a conventional power generator in vehicles, owing to its high energy conversion efficiency and ecologically benign products [1–3]. The oxygen reduction reaction (ORR) occurring at the cathode of a fuel cell has slow kinetics, and therefore limits the performance of the fuel cell. The most common catalyst to accelerate the ORR is platinum nanoparticles supported on carbon (Pt/C). However, the high cost of Pt impedes the widespread application of fuel cells. Although the use of Pt-alloy catalysts has been considered as an alternative strategy to increase the ORR activity with less Pt [4–6], it is not a permanent solution, as Pt is scarce.

For the complete replacement of Pt in the cathode, non-precious metal catalysts (NPMCs) have recently been studied [7–9]. In this regard, anion exchange membrane fuel cells (AEMFCs) also have been highlighted, because the ORR on NPMCs tends to be faster in alkaline conditions than acidic conditions [2,3]. Covalent doping with heteroatoms is a common method to achieve ORR activity using carbon materials. Changes in the charge and spin densities of carbon atoms have been considered as the origin of the ORR activity of the heteroatom-doped carbon materials [10–13]. Meanwhile, incorporating metal in heteroatom-doped carbon leads to greater enhancement of the ORR activity. Since Jasinski's work [14], composites of nitrogen-doped carbon-based materials and third-row transition metals (i.e., Fe or Co) have been developed as ORR catalysts [7,15,16]. In particular, iron-

containing nitrogen-doped carbons (Fe/N/Cs) have shown outstanding ORR activity. Fe/N/C is generally synthesized by pyrolyzing a mixture of Fe, N, and C precursors at a high temperature (> 800 °C) in an inert atmosphere [8,9,17].

The generation of active catalytic sites is important for the development of NPMCs. The Fe-N_x/C site, at which a single Fe ion is coordinated to N functionalities at the edge of a carbon basal plane, is a molecule-type active site that is considered as the main active site for ORR in Fe/N/C [18–21]. The Fe-N_x/C site accelerates the ORR significantly under alkaline conditions. The key factors for the ORR occurring at the Fe-N_x/C site are the Fe^{3+}/Fe^{2+} transition potential and stabilization of the peroxide intermediate. In alkaline conditions (pH > 12), the transition of Fe^{3+} to Fe^{2+} occurs at high potential and the anionic peroxide intermediate (HO_2^-) is strongly stabilized on the Fe-N_x/C site; therefore, the overpotential of ORR is reduced and a desirable $4e^-$ ORR pathway is highly preferred [18,22]. However, because the catalyst that contains the Fe-N_x/C site is synthesized by heat-treatment of a precursor mixture containing Fe, N, and C at a high temperature (> 800 °C), at which the Fe-N_x/C site is not stable, the development of a controlled synthesis is required to dominantly generate the Fe-N_x/C site in the catalyst [22–25]. An intuitive way to generate the site is to use precursors that are analogous to the Fe-N_x/C site, where an Fe ion is coordinated to nitrogen functionalities in aromatic rings (Fe-CNAR precursor) [7,15,17]. Even if the molecular structure of the precursor is changed significantly during the high-temperature pyrolysis, this approach can be expected to generate more Fe-N_x/C molecule-type catalytic sites than using a simple mixture of the Fe, N, and C precursors with no coordination.

To practically utilize an NPMC with Fe-N_x/C active sites in the cathode of the fuel cell, the accessibility of the active site should be considered carefully. Fuel cell cathodes made of carbon-based NPMCs usually have high mass-transport resistance, because most of the active sites are buried inside the catalyst particles, and because the catalyst layer is relatively thick owing to the low volumetric activity of the NPMC [15]. The high mass-transport resistance, which is exerted on the reactants as they approach the catalytic sites, reduces the reaction kinetics and makes the utilization of active sites inefficient. This feature appears distinctly in a single-cell performance test performed using a membrane electrode assembly (MEA) [26–28]. Many cathodes made of NPMCs have exhibited much lower performances than that of Pt/C in a single-cell system, even if the NPMCs showed comparable or superior ORR kinetic activities to Pt/C in half-cell tests with a rotating-disk electrode (RDE) [28]. Although there have been a few reports of MEAs with NPMC cathodes exhibiting higher performance than MEAs with Pt/C cathodes, in the case of fuel cells using alcohols as the fuel fed into the anode, the current densities and power densities are too low [29–31]. To minimize the mass-transport resistance of an NPMC and to enable the catalyst to exhibit the best performance in a practical fuel cell system, the nanoporosity of the NPMC must be controlled.

An ordered mesoporous structure can provide both high surface area and facile mass transport in pores [32–34], and is therefore highly desirable in practical NPMCs [15,28,35]. The hard-template method is a common strategy to synthesize mesoporous materials with a negative-replica structure of a porous template (e.g., mesoporous silica) [36–40]. However, the synthesis process is time-consuming and involves tedious steps because of the required formation and removal of the template material. Meanwhile, soft-template synthesis is a simple and useful alternative to fabricate a mesoporous material. This method requires very simple steps, including the assembly of a structure-directing agent (SDA) and precursors of target materials, and subsequent pyrolysis [41–43]. Unfortunately, the self-assembly of the SDA is sensitive to the interaction of the assembly agents; therefore, the direct incorporation of the precursor to form the Fe-N_x/C sites has been difficult. It is highly desirable to develop a soft-template synthesis for a mesoporous NPMC with Fe-N_x/C sites by incorporating Fe-CNAR precursors during the self-assembly step. In addition to the high kinetic activity and mass

transport of the catalyst, simplicity of the synthesis can be achieved.

Herein, we report a simple soft-template process to synthesize an ordered mesoporous NPMC with Fe-N_x/C active sites (m-FePhen-C) by the direct incorporation of an Fe-CNAR precursor (complex of Fe^{2+} ion and 1,10-phenanthroline (phen)) in the block co-polymer self-assembly. Compared to previous works that involved impregnating a preformed mesoporous template with catalytic site precursors, heating the composite, and removing the template to make mesoporous Fe/N/C, the synthesis reported in this work is much simpler, in that the active sites and ordered mesoporous structure are formed simultaneously in a single step [15,16,35]. Moreover, this is notably the first report of an Fe-CNAR precursor being directly incorporated in a block co-polymer-assisted soft-template method for the synthesis of mesoporous Fe/N/C. Many reports about NPMCs have reported only the kinetic activities of catalysts measured in the half-cell system, even though the catalytic performance in a practical single-cell system can be totally different from that in a half-cell system. Desirably, m-FePhen-C showed high catalytic performance both in half-cell and single-cell systems [28]. The kinetic activity measured in the half-cell system was higher than that of Pt/C, and an MEA with an m-FePhen-C cathode showed 40% higher power density than did an MEA with a commercial Pt/C cathode in single-cell performance tests, in which the catalyst loadings and electrode thicknesses were comparable.

2. Experimental

2.1. Synthesis of m-FePhen-C

Pluronic F127 (Aldrich) 0.64 g was dissolved in a co-solvent of ethanol (2.23 mL) and 0.2 M HCl (0.22 mL). The Fe(phen)$_3$Cl$_2$ complex was prepared separately by mixing FeCl$_2$·4H$_2$O (93 mg) and 1,10-phenanthroline (253 mg) in the co-solvent of ethanol (16.9 mL) and 0.2 M HCl (1.67 mL). Resol (0.26 g) [44], tetraethylorthosilicate (TEOS) (Aldrich, 0.892 mL), and the Fe(phen)$_3$Cl$_2$ complex solution (7 g) were added to the polymer solution. After being stirred for 1 h, the solution was poured to a dish. The solvent was evaporated at 50 °C, and the dish was stored in an oven at 100 °C for 24 h. The obtained polymeric nanocomposite was pyrolyzed at 900 °C for 2 h (ramping rate: 1 °C min^{-1} to 350 °C; 350 °C was maintained for 3 h; 1 °C min^{-1} to 600 °C; 5 °C min^{-1} to 900 °C). Decomposition of F127 occurs severely around 350 °C, and polymeric phenolic resin (obtained by polymerization of resol) is converted to a conductive carbon structure or is partly decomposed below 600 °C [42,45]. To make such intense changes take place slowly and not affect to the catalyst structure, we increased the temperature slowly (1 °C min^{-1}) below 600 °C. Keeping the temperature at 350 °C for 3 h was for the complete decomposition of F127. Above 600 °C, the structure of carbon crystallite is changed [45]. Because this change is less intense than the changes occurring below 600 °C, this change is less likely to affect the catalyst structure. Therefore, we increased the temperature fast above 600 °C (5 °C min^{-1}). Silica in the framework was removed by etching in 10 wt. % HF solution (25 °C, 2 h). m-FePhen-C was finally obtained by the second heat-treatment at 900 °C in Ar for 1 h (ramping rate: 3 °C min^{-1}). The second heat-treatment was required to remove the anions or impurities that could bind to the active sites during the etching process [46]. Even if the removal of anion or impurities is not an intense change that affects the structure of the catalyst, the water or oxygen molecules adsorbed on the catalyst surface can damage the catalytic site during the heat-treatment when the sample is heated too fast from room temperature to 900 °C. Therefore, we used an intermediate ramping rate of 3 °C min^{-1} in the second heat-treatment.

2.2. Synthesis of sample set for comparison of electrochemical catalytic activity

b-FePhen-C was synthesized by the same procedure as that of the

synthesis of m-FePhen-C, excluding the addition of F127. m-Phen-C was synthesized by the same procedure of as that of the synthesis of m-FePhen-C, excluding the addition of $FeCl_2 \cdot 4H_2O$. sm-FePhen-C was synthesized by a hard-template method with SBA-15 mesoporous silica template. Resol 0.5 g and $Fe(phen)_3Cl_2$ 0.269 g were impregnated into the pores of SBA-15 by the repetition of an incipient wetness impregnation method. A heat-treatment profile and etching process were conducted identically with the synthesis of m-FePhen-C. FePhen-MpC was synthesized by the heat-treatment of $Fe(phen)_3Cl_2$ loaded into microporous carbon. 0.2 g of Ketjen black EC 300J and 0.215 g of Fe $(phen)_3Cl_2$ were dispersed in ethanolic solution containing 10 v/v% 0.2 M HCl, and the solvent was evaporated. A subsequent heat-treatment profile and etching process were conducted identically with that of synthesis of m-FePhen-C.

2.3. Material characterization

UV/Visible light spectroscopy was performed using an Agilent 8340. Small angle X-ray scattering (SAXS) patterns were measured at the 4C SAXS II beamline at the Pohang Accelerator Laboratory (PAL, Korea). A N_2-adsorption experiment was conducted to investigate the surface area and pore size distribution using a Micromeritics Tristar II 3020. X-ray photoelectron spectroscopy (XPS) was performed using a Kratos Nova VG Scientific Escalab 250 (Al Kα). Inductively coupled plasma spectroscopy was performed using a Shimadzu ICPE-9000. Raman spectroscopy was performed by a Horiba Jobin Yvon (LabRam Aramis) with a 514 nm Ar-ion laser. Elemental analysis was performed by VarioEL (III) (ANALYSENSYSTEME GMBH). Microscopic images were obtained using a JEOL JEM-2010 transmission electron microscope (TEM) and a Hitachi-S-4200 field emission-scanning electron microscope (FE-SEM). X-ray absorption spectroscopy (XAS) data of the Fe K-edge of the samples were collected in transmission mode at room temperature at the BL10C in PAL (Korea). The sample was fixed on a sample holder using Kapton® tape. The XAS data were analyzed by Athena and Artemis software. X-ray absorption near edge structure (XANES) was used for the chemical state analysis and coordination symmetry, and extended X-ray absorption fine structure (EXAFS) was used to elucidate the local geometric factor around iron. XANES analysis was conducted after background subtraction and normalization. The EXAFS signals for the Fe K-edge of the samples were extracted and were Fourier-transformed (FT) over the k-space range of 2.5–10 Å^{-1}, using k^3 weight and a Hanning window. X-ray diffraction (XRD) data were obtained by using a Max-2500 diffractometer (RIKAGU, Cu Kα, 1.5418 Å).

2.4. Electrochemical characterization

2.4.1. Half-cell test

The obtained catalyst was milled by agate mortar and ball-milling with zirconia balls. A catalyst slurry was made by dispersing the catalyst powder and Nafion® ionomer in 2-propanol. The weight ratio of Nafion® ionomer to catalyst powder was 0.6. The slurry was deposited on a glassy carbon electrode (0.19625 cm^2) by micropipette, and the loading amount on the electrode was 160 μg. ORR polarization curves were obtained by a linear sweep voltammetry method in O_2-purged 0.1 M KOH solution with 5 mV s^{-1} (anodic scan) using an RDE (1600 rpm). The background current was measured in an Ar-purged 0.1 M KOH solution and subtracted from the current measured in the O_2-purged solution. An Ag/AgCl (in saturated KCl) electrode and a Pt wire were used as reference and counter electrodes, respectively. For the electrochemical poisoning test, a solution with 10 mM KCN and 0.1 M KOH was used.

2.4.2. Preparation of MEAs

A catalyst-coated membrane (CCM) was fabricated by a spray method for MEA. The anode used for all the AEMFC tests in this work was 40 wt.% Pt/C (Johnson Matthey Co.) with a catalyst loading of

0.5 mg cm^{-2}. The synthesized m-FePhen-C served as the cathode catalyst with catalyst loading amounts of 1, 2, and 4 mg cm^{-2}. For comparison, 40 wt.% Pt/C (Johnson Matthey Co.) and sm-FePhen-C were used as cathode catalysts with a loading of 1 mg cm^{-2}. The catalyst loading was confirmed by measuring the mass of the membranes before and after the deposition of the catalyst layer. All the catalysts were dispersed in a mixture of isopropyl alcohol, deionized water, and ionomer (AS-4, Tokuyama) to prepare the catalyst ink, which was then ultrasonicated for 10 min and sprayed onto A901 membrane (Tokuyama). The CCM was dried for 1 day before the single-cell assembly. Carbon paper containing microporous layers (MPLs; 35BC, SGL) was used as a gas diffusion layer placed on the cathode and anode sides of the anion exchange membrane. The MEAs were inserted into a single-cell unit that had a graphite plate with a serpentine gas flow channel (5 cm^2 geometric area).

2.4.3. Single-cell test

Activation and polarization tests of the assembled single-cells were performed using a fuel cell test system (CNL energy Co., Korea). For the activation, humidified gases were fed into the fuel cell with constant flows to humidify the membrane. Polarization curves were measured using the current-sweep method with a current sweep rate of 10 mA cm^{-2} s^{-1}. The current was reset to zero when the cell voltage reached 0.3 V. The test was conducted using fully humidified H_2 and O_2, which were supplied to the anode and cathode, respectively. The total outlet pressure was 180 kPa. The cell temperature was maintained at 50 °C during the activation and the polarization tests. In addition, for the performance comparison under the back-pressure condition suggested by the US Department of Energy, the oxygen gain test was conducted with a back-pressure of 150 kPa. The cell temperature was maintained at 50 °C during the activation and the polarization tests.

3. Result and discussions

3.1. Synthesis and analysis of materials

The synthetic procedure for m-FePhen-C is illustrated in Fig. 1. The ordered nanostructure of the catalyst was obtained by the selective interaction of resol (carbon precursor) [44], hydrolyzed TEOS (silica precursor), and $Fe(phen)_3Cl_2$ (catalytic site precursor) with the Pluronic F127 block co-polymer (poly(ethylene oxide)$_{106}$-poly(propylene oxide)$_{70}$-poly(ethylene oxide)$_{106}$).

$Fe(phen)_3Cl_2$ was prepared by mixing $FeCl_2$ and 1,10-phenanthroline in ethanolic solution, and it was then added to a casting solution that contained the carbon and silica precursors and F127. The formation of the $Fe^{2+}(phen)_3$ complex was confirmed by UV/Visible light absorption spectroscopy. The spectrum (Fig. 2a) obtained from the casting solution just before it was casted in the dish showed a distinct maximum peak near the wavelength of 510 nm; this peak and the red color of the solution demonstrate that an $Fe^{2+}(phen)_3$ complex had formed and was not affected by the other solutes. This feature is advantageous for the formation of many Fe-N$_x$/C molecule-type catalytic sites during subsequent carbonization.

During the evaporation-induced self-assembly (EISA) step after casting, an ordered nanostructure with hexagonal symmetry was formed by microphase separation of the hydrophobic polypropylene oxide (PPO) block and the hydrophilic polyethylene oxide (PEO) block of F127. Subsequently, hydrophilic carbon and silica precursors were assembled with the PEO block to form the framework of the mesoporous structure. The $Fe^{2+}(phen)_3$ complex was also co-assembled in the PEO block compartment without destruction of the ordered structure. The size of the $Fe^{2+}(phen)_3$ complex as measured by a molecular model was 1.14 nm (Fig. S1). The PEO block of F127 had a root-mean-square end-to-end distance ($R_{0,PEO}$, Eq. (1)) of 6.96 nm, as defined by the following [47].
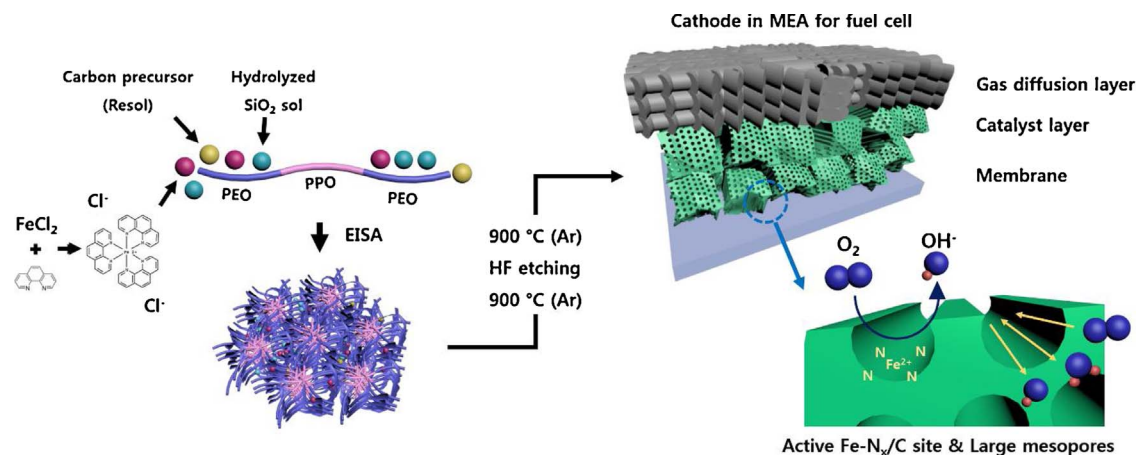
Fig. 1. Schematic illustration of the synthesis of m-FePhen-C.

$$R_0 = aN^{1/2} \tag{1}$$

where $a = 0.7$ for PEO in F127, and N is the degree of polymerization; thus, the co-assembly of the complex with the PEO block in F127 was entropically favored.

The SAXS pattern of the as-synthesized form of m-FePhen-C (m-FePhen-C-as-syn) that had been obtained using the EISA process showed peaks at the relative scattering vector positions of the first-order maxima, $1:3^{1/2}:4^{1/2}$, which indicated the formation of a 2-D hexagonal *p6mm* structure (Fig. 2b) [48]. Heat-treatment at 900 °C converted the PPO block part to mesopores, and converted the PEO block part to pore walls consisting of carbon and silica. $Fe^{2+}(phen)_3$ was converted to catalytic sites for the ORR at the walls. After subsequent HF etching to remove the silica framework and a second heat-treatment in Ar, the final m-FePhen-C sample was obtained. Although the SAXS peaks were shifted to high vector positions owing to shrinkage during the heat-treatment, the conserved relative peak positions indicated that the ordered structure was maintained. When b-FePhen-C was synthesized without F127, the SAXS pattern showed no distinct

peak; this observation indicates that the ordered structure was induced by the self-assembly of F127. A large mesopore size (9.3 nm) and narrow pore size distribution of m-FePhen-C were revealed by the N_2 physisorption experiments (Fig. 2c). The surface area was as large as $1437 \text{ m}^2 \text{ g}^{-1}$ owing to the contribution of both mesopores and micropores. This structural feature is appropriate to provide many reaction sites and facile mass transport in the catalyst particle. Meanwhile, b-FePhen-C had a very low surface area ($102 \text{ m}^2 \text{ g}^{-1}$) and did not exhibit no porosity.

The ordered mesoporous structure of m-FePhen-C was also observed by SEM and TEM (Fig. 3a–c). The sample grid for TEM analysis was prepared by a microtoming process that embedded the sample particle in an epoxy resin and sliced the particle to observe the inside of the particle clearly. Fig. 3a and b shows the side view of the hexagonally arranged cylindrical pores, and Fig. 3c shows the top view of the cylindrical pores (see also Fig. S2 in the supplementary data). Electron microscopy images (Fig. 3a–c) show that the self-assembled structure induced by the block co-polymer was successfully converted to the ordered mesoporous structure after the heat-treatment. The distribution
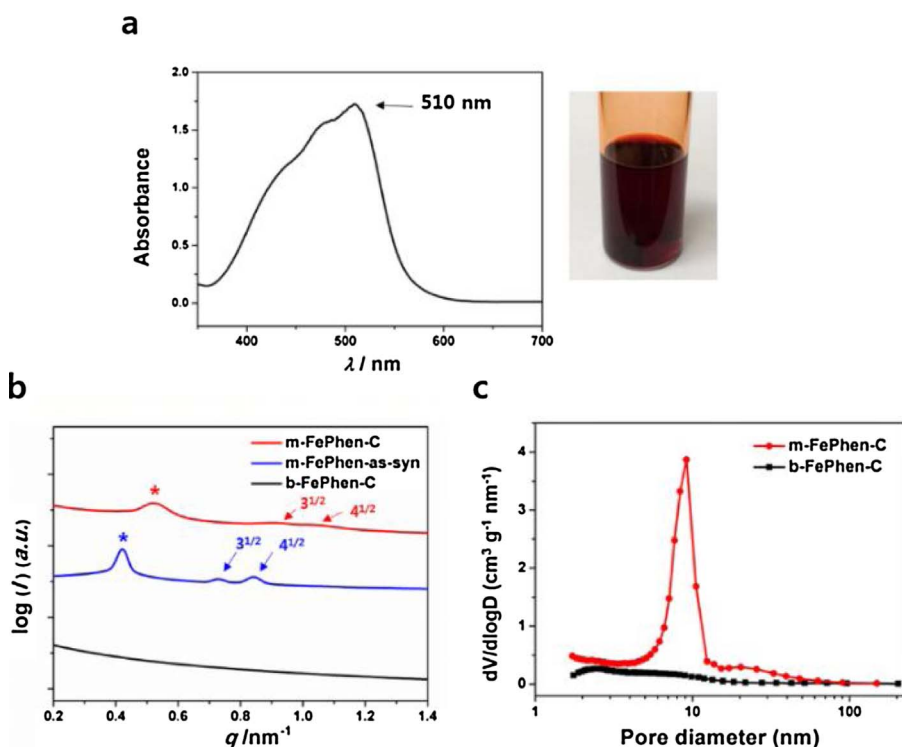

Fig. 2. (a) UV/Visible light absorption spectroscopy and photo image of casting solution of m-FePhen-C. (b) SAXS patterns of m-FePhen-C, m-FePhen-as-syn, and b-FePhen-C. (c) Pore size distribution plots of m-FePhen-C and b-FePhen-C.
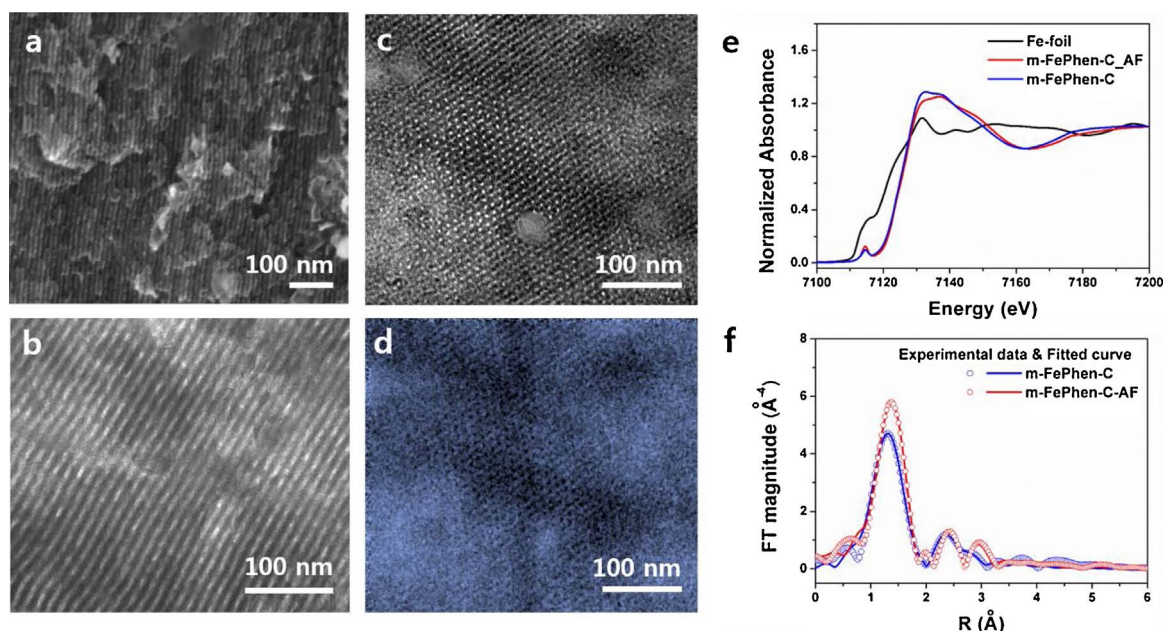
Fig. 3. (a) SEM and (b) TEM images providing a side view of cylindrical pores in m-FePhen-C. (c) TEM images providing a top view of cylindrical pores of m-FePhen-C. (d) EELS mapping results for Fe over the same area as Fig. 3c. The blue spots indicate the distribution of Fe element. (e) XANES curves for m-FePhen-C_AF, m-FePhen-C, and reference Fe-foil. (f) FT-EXAFS curves and the fitted results for m-FePhen-C_AF and m-FePhen-C. (For interpretation of the references to colour in this figure legend, the reader is referred to the web version of this article.)

of iron-based catalytic sites in the mesopore wall was visualized by electron energy loss spectroscopy (EELS) elemental mapping (Fig. 3d). We could see that the Fe elements were located along the mesopore wall, and that large inorganic particles resulting from the sintering of Fe were not observed.

Fe K-edge XAS spectra are presented in Fig. 3e–f. XANES can provide information about the chemical state and coordination symmetry of the target elements. The XANES region in the XAS spectra (Fig. 3e) of m-FePhen-C and m-FePhen-C_AF (i.e., the sample obtained just after the first heat-treatment) showed higher white-line intensities than that of the Fe-reference foil, and the absorption edges also shifted to higher energy as compared to that of the reference foil; these results indicate that the Fe in m-FePhen-C had a valence oxidation state rather than metallic Fe (0) state. In the pre-edge region, a distinct small peak at 7114 eV was shown both in the m-FePhen-C and m-FePhen-C_AF spectra. This peak was derived from the transition from 1s to 3d, which is dipole-forbidden but quadrupole-allowed; this peak indicated that the dominant coordination geometry around Fe was close to a square pyramidal structure [49]. This coordination geometry in which the metal center was displaced out of square planar, which was formed by nitrogen functionalities in the carbon basal plane, implied the existence of axial ligation or molecular adsorption on the metal center.

EXAFS provided information about the local geometric factor around Fe, and showed the dominant presence of the Fe-N$_x$/C molecule-type active site. The FT-spectra and the fitted results of the radial distribution of m-FePhen-C and m-FePhen-C_AF (Fig. 3f) showed main peaks at ~1.4 Å, caused by backscattering from the first coordination shell. These peaks can be assigned to Fe-N coordination bonds or Fe-O bonds derived from molecular adsorption. The coordination number of the Fe-N bond in m-FePhen-C obtained by fitting was 4.09; this value indicates that the coordination environment of Fe in m-FePhen-C was similar to that of the Fe-N$_4$/C site, which has been proposed as an ORR active site [18,19,50]. The obtained coordination number and bond length were similar in m-FePhen-C and m-FePhen-C_AF (Table S1); this similarity implied that the Fe-N coordination was formed during the first heat-treatment, and was stable in the post-treatment processes including the acid treatment and a second heat-treatment. A fitting analysis revealed the existence of adsorbed oxygen on the Fe center as

implied by the XANES analysis (Table S1). The additional parameters obtained by the fitting analysis of the first coordination shell are summarized in Table S1.

Generally, an Fe–Fe metallic bond peak, which originates from Fe metallic particles, is shown near 2.2 Å in the FT spectra (Fig. S3) [51]. No distinct peak was observed in this vicinity of this region in the FT spectra of either m-FePhen-C or m-FePhen-C_AF. Carbonization concurrent with the formation of catalytic sites in the confined space with a rigid silica framework in the mesoporous wall prevented significant undesirable sintering of Fe to metallic particles. This feature is highly advantageous to convert the Fe elements in a catalyst precursor to active Fe-N$_x$/C sites without the formation of metallic particles for a highly active ORR catalyst. Moreover, in the XRD patterns for m-FePhen-C and m-FePhen-C_AF, distinct peaks for Fe metal or Fe-oxide phase were not observed (Fig. S4).

The nitrogen functionalities of m-FePhen-C were analyzed by the N1s spectrum obtained by XPS (Fig. 4). The N1s spectrum was deconvoluted to four peaks: those for pyridinic N (398.8 eV) [52–54], pyrrolic N (400.2 eV) [54,55], graphitic N (401.2 eV) [54,56], and oxidized N (402.3 eV) [54,57]. Pyridinic and pyrrolic N refer to the N atoms incorporated in six- and five-membered heterocyclic aromatic rings, respectively [58,59]. Because pyridinic N is believed to be the N functionality at Fe-N$_x$/C sites, the pyridinic N content was closely
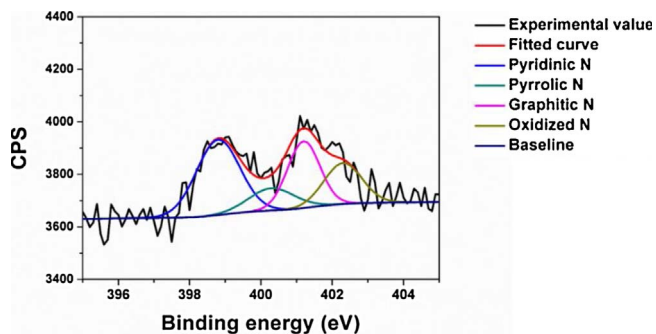

Fig. 4. N1s XPS spectra for m-FePhen-C and deconvoluted peaks. The nitrogen functionalities of m-FePhen-C consist of pyridinic N, pyrrolic N, graphitic N, and oxidized N.

related to the number of Fe-N_x/C sites [54,55,59]. Graphitic N refers to a nitrogen incorporated in the graphene plane, bonded to three carbon atoms [58]. Oxidized N is bonded to two carbon atoms and one oxygen atom [58]. The contents of the N functionalities were 41% of pyridinic N, 13% of pyrrolic N, 27% of graphitic N, and 19% of oxidized N. The high content of pyridinic N in m-FePhen-C implied the predominant formation of Fe-N_x/C sites. The weight percentages of Fe and N in m-FePhen-C as measured by inductively coupled plasma-optical emission spectroscopy and CHN elemental analysis were 0.24 wt.% and 2.2 wt. %, respectively.

We also investigated the effect of the heat-treatment temperature on the carbon structure and the Fe-centered active site structure of the Fe/N/C catalyst. Raman spectroscopy results of the catalysts that were synthesized by heat-treatment at 700, 800, 900, and 1000 °C showed D- and G-band peaks near 1335 and 1600 cm^{-1}, respectively, which are usually exhibited by conductive carbon materials (Fig. S5a). The peak intensity ratio of the D-band and G-band (I_D/I_G) increased slightly as the temperature increased, owing to the randomly formed carbon crystallites (Fig. S5b), as reported in previous studies about the microstructure changes of cured phenolic resin during the pyrolysis [45,60,61].

Up to 900 °C, the coordination environment around Fe did not changed significantly, as demonstrated by the FT-EXAFS signals (Fig. S6). Only the selectively formed Fe-N coordination bond peak was distinctively seen near 1.4 Å. However, in the FT-EXAFS signal of the 1000 °C heat-treated catalyst, a highly intense peak indicating the presence of an Fe–Fe metallic bond appeared near 2.2 Å. This implied that the structure of Fe-N_x/C active sites can be maintained stably up to 900 °C, but a higher heat-treatment temperature leads to easy sintering of the Fe elements in Fe-N_x/C sites to Fe metallic particles.

3.2. Electrochemical characterization in half-cell system

To evaluate the ORR activity of m-FePhen-C, an RDE test was performed in the half-cell system (Fig. 5a). To identify the factors that enhance the ORR in m-FePhen-C, several samples were prepared: (i) b-FePhen-C, (ii) m-Phen-C (synthesized by the same process as that for m-FePhen-C preparation but excluding the Fe precursor), (iii) FePhen-MpC, (heat-treated $Fe^{2+}(phen)_3$ complex with a microporous carbon support), and (iv) commercial Pt/C (40 wt.%, Johnson-Matthey). Interestingly enough, the noble metal-free m-FePhen-C catalyst showed a slightly higher ORR activity than did Pt/C, represented by a half-wave potential of 0.901 V. The ORR onset potential of m-FePhen-C was also

as high as 1.00 V, and the current density plateau derived from the diffusion limitation was close to the theoretical value of 5.5 mA cm^{-2}. The polarization curve for m-Phen-C showed the importance of the presence of Fe (Fig. 5a) in addition to N-doping. Although the same N precursor was used, the onset potential of m-Phen-C was very low and the diffusion-limiting current did not reach the ideal value; this deficit indicated that the direct O_2-reduction pathway with four-electron transfer was not preferred by this catalyst.

A comparison of the ORR polarization curves of m-FePhen-C, b-FePhen-C, and FePhen-MpC showed the advantage of the mesoporous structure of the NPMC (Fig. 5b). b-FePhen-C and FePhen-MpC had low surface areas (Table S2), owing to the poor porosity, and therefore showed low ORR activity, even if the same catalyst precursor as that for m-FePhen-C was used. The surface area of the microporous carbon (Ketjen black: 812 $m^2\,g^{-1}$), used in the synthesis of FePhen-MpC, was drastically decreased, because the small micropores were easily blocked by the pyrolyzed product of the catalyst precursor.

We also observed the heat-treatment temperature dependence of the ORR activity of m-FePhen-C. The ORR activity was optimal when the heat-treatment temperature was 900 °C. The catalysts prepared by heat-treatment with a temperature lower or higher than 900 °C showed significantly lower ORR activity than that obtained by m-FePhen-C (900 °C heat-treated sample) (Fig. S7). As shown in Fig. S5, the peak intensity ratio (I_D/I_G) obtained by Raman spectroscopy increased with increasing heat-treatment temperature, as observed in the general carbon materials derived from phenolic resin [45,61]. This meant that the size of the carbon crystallite size decreased as the heat-treatment temperature increased [45,60,62]. The increase in the ORR activity of the synthesized Fe/N/C heat-treated up to 900 °C is caused by the ORR activity of the Fe-N_x/C site in Fe/N/C catalyst increasing as the carbon crystallite size decreases [18,62]. However, when the heat-treatment temperature was as high as 1000 °C, the Fe was sintered to metallic particles, as demonstrated by the EXAFS data (Fig. S6). Therefore, the number of the Fe-N_x/C active sites decreased significantly and the ORR activity was decreased even if the carbon crystallite size decreased, as indicated by the high I_D/I_G value (Fig. S5b). The decrease in the number of Fe-N_x/C sites in the 1000 °C heat-treated sample was also confirmed by XPS analysis of the N1s spectra (Fig. S8). Up to heat-treatment temperatures of 900 °C, the pyridinic N contents, closely related to the number of Fe-N_x/C sites, were maintained at similar values (Fig. S9). However, the content of pyridinic N was significantly lower for the 1000 °C heat-treated sample than those in the other samples (Fig. S9).
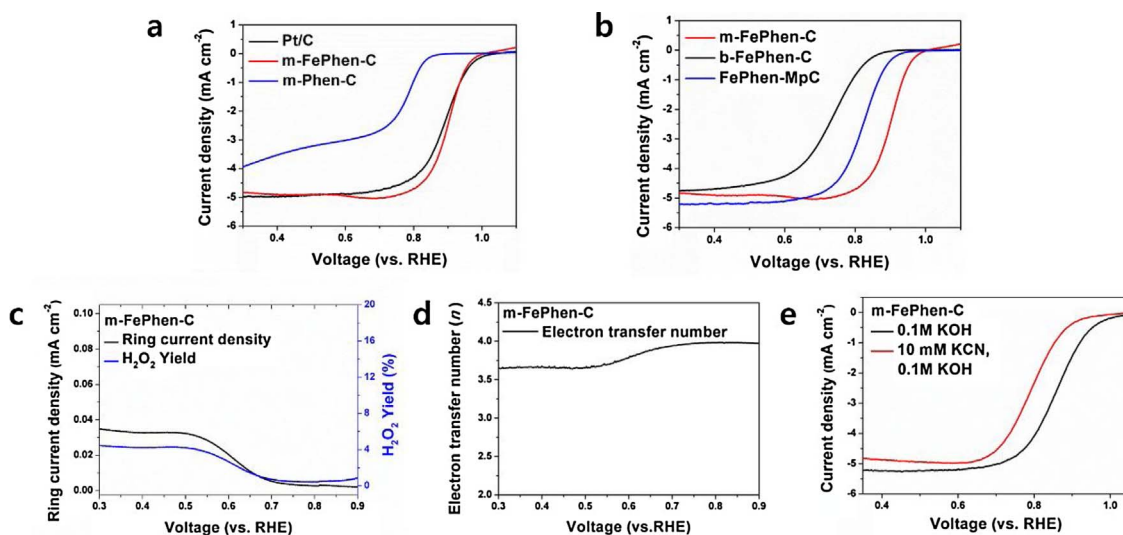

Fig. 5. (a) ORR polarization curves for Pt/C (40 wt.%), m-FePhen-C, and m-Phen-C. (b) ORR polarization curves for m-FePhen-C, b-FePhen-C, and FePhen-MpC. (c) Ring current density and H_2O_2 production yield of m-FePhen-C obtained by RRDE experiment. (d) Electron transfer number of ORR on m-FePhen-C catalyst. (e) ORR polarization curves for m-FePhen-C obtained in 0.1 M KOH and 10 mM KCN/0.1 M KOH solutions. The rotation speed of the electrode was 1600 rpm in all experiments.

The efficiency of the ORR process on m-FePhen-C was evaluated using a rotating ring-disk electrode (RRDE) experiment and Koutecky-Levich plots. The H_2O_2 oxidation current detected at the ring electrode was negligible compared to that at the disk current. The H_2O_2 production yield was < 5% over the entire potential range (Figs. 5 c and S10). The calculated electron transfer number from the ring current was very close to 4.00 (Fig. 5d) which means that the reduction of O_2 occurred preferentially by the direct four-electron pathway. This catalytic behavior was observed similarly in the analysis using the Koutecky-Levich plots, which showed a linear relationship between the inverse current density and the fast inverse square root of the angular velocity (Fig. S11), in agreement with the Koutecky-Levich equation (Eq. S1). The high selectivity of the four-electron pathway on m-FePhen-C was also confirmed by the electron transfer number calculated from the slopes of the Koutecky-Levich plots (Fig. S11b). The chronoamperometry used to investigate the current retention demonstrated that m-FePhen-C was more durable than Pt/C in catalyzing ORR under alkaline condition (Fig. S12).

This excellent ORR activity of m-FePhen-C was attributed to (i) the highly active Fe-N_x/C sites derived from the Fe^{2+}(phen)$_3$ complex, and (ii) the large number of active sites provided by the mesoporous structure. In addition to the XAS analysis, the formation of Fe-N_x/C sites was confirmed by poisoning tests using the cyanide ion (CN^-), which poisons the metal center of nitrogen-containing macrocycles [63]. When the electrode fabricated by m-FePhen-C was tested in 0.1 M KOH aqueous solution containing 10 mM KCN, the onset potential and half-wave potential shifted remarkably to the negative side (half-wave potential shift: − 69 mV, Fig. 5e) compared to those obtained in 0.1 M KOH solution. The similar diffusion-limiting current indicated that the decrease in the ORR activity was not caused by a change of environment, such as the O_2 solubility or a solution viscosity. This result indicated that Fe-N_x/C sites were formed and contributed significantly to the ORR activity.

3.3. Single-cell tests

Polarization and power density curves (Fig. 6a) were obtained by a single-cell test conducted on AEMFCs with m-FePhen-C and Pt/C 40 wt. % cathode catalysts. The amount of m-FePhen-C in the cathode was varied from 1 to 4 mg cm^{-2}. The optimized maximum power density was obtained for the catalyst loading of 1 mg cm^{-2}. At the high voltage region, where the cell voltage loss is dominated by charge transfer in the catalytic reaction [64], the voltage loss decreased as the catalyst loading amount increased, because the number of reaction sites increased. When 4 mg cm^{-2} of m-FePhen-C was loaded, the activation loss was similar to that of the Pt/C 40 wt.% cathode (the magnified figure of the kinetic-controlled region in the I–V curves is presented in Fig. S13.). This result indicated that the Fe-N_x/C catalytic sites were highly active for ORR in the single-cell system as well. When the voltage was < 0.7 V, the voltage loss became significant as the catalyst loading increased, mainly owing to the increase in ohmic and mass transfer loss as the thickness of the catalyst layer increased. Because the ratio of the catalyst layer thickness to the membrane thickness is high in AEMFCs, the resistance from ion and mass transport in the catalyst layer is more significant compared to that in the proton exchange membrane fuel cell (PEMFC) [65,66].

When the catalyst loading of m-FePhen-C (1 mg cm^{-2}) was identical with that of Pt/C 40 wt.% (1 mg$_{Pt}$ cm^{-2}), the m-FePhen-C cathode showed a higher performance mainly in the ohmic and mass transfer controlled region (Fig. 6c), even though the catalyst layer of m-FePhen-C cathode (40 μm) was slightly thicker than that of the Pt/C cathode (36 μm) (Fig. S14a,d). The maximum power density for the AEMFC with the m-FePhen-C cathode was 272 mW cm^{-2}, which was 40% higher than that for the AEMFC with the Pt/C cathode and was comparable to the performance reported for another superior NPMCs (Table S3). Even though the power density obtained for the MEA with m-

FePhen-C cathode was not as high as the highest power density obtained from Pt/C cathodes among the reported results (Table S3), the result is highly meaningful because it is very rare that an MEA with an NPMC cathode exhibits a higher power density than MEA with Pt/C cathode when their electrode thicknesses and catalyst loadings are comparable. This result is clear evidence of the advantage of an NPMC with mesoporous structure with a large pore size in a fuel cell cathode. The interparticle pores in the m-FePhen-C cathode also had an important function in the mass transfer of oxygen and water in the thick catalyst layer [65,67]. Owing to the relatively large particle size of m-FePhen-C, its cathode had larger interparticle pores than those in the Pt/C cathode (Fig. S14e,f). The enhancement of the mass transport also could be confirmed by the oxygen gain, expressed by the difference between potentials observed for the oxygen-fed fuel cell and the air-fed fuel cell [68–70]. The oxygen gain is a general indicator for mass transport loss of the catalyst layer. As seen in Fig. S15, the AEMFC with the m-FePhen-C cathode showed a much lower oxygen gain compared to that of the Pt/C 40 wt.% cathode, indicating that m-FePhen-C has a more favorable catalyst structure for facile mass transport than Pt/C when both catalyst layers have similar thicknesses of approximately 40 μm. This result is also in good agreement with those depicted in Fig. 6. In the single-cell test conducted for the AEMFC system, m-FePhen-C catalyst also exhibited higher durability than Pt/C cathode catalyst (Fig. S16).

sm-FePhen-C is a mesoporous catalyst synthesized from the same precursor as m-FePhen-C. (Note that sm-FePhen-C was synthesized through the hard-template method, which requires multiple steps.) sm-FePhen-C had smaller mesopores than m-FePhen-C (main pore size: 3.7 nm, Fig. S17). A performance comparison of m-FePhen-C and sm-FePhen-C cathodes in the AEMFC system gives information about the effect of mesopore size in NPMCs on the single-cell performance (Fig. 6b). sm-FePhen-C showed an almost similar ORR kinetic activity to m-FePhen-C (Fig. S18). In the single-cell performance test, the two cells showed similar activation loss behaviors. However, at voltages below 0.7 V, the sm-FePhen-C cathode showed higher ohmic and mass transport losses than did the m-FePhen-C cathode (Fig. 6b and d). This result demonstrated that the pore size of catalysts had a strong influence on the ohmic loss and mass transport in the catalyst layer in a single-cell [28,67]. Compared to the small mesopores, large mesopores can transport the reactant and product more easily even after the ionomer is incorporated in the pores. Furthermore, the incorporation of the ionomer can be more efficient in large pores, and therefore, ohmic loss derived from discontinuity of the ionomer can be minimized. The sm-FePhen-C-based AEMFC showed a much lower peak power density than did the m-FePhen-C-based AEMFC.

4. Conclusions

Ordered mesoporous NPMC for ORR (m-FePhen-C) was synthesized by the direct incorporation of an Fe^{2+}(phen)$_3$ complex into a block copolymer assembly. m-FePhen-C catalyst with the Fe-N_x/C molecule-type active sites that were generated by the designed catalyst precursor exhibited a higher ORR kinetic activity than did Pt/C in the half-cell tests. A well-developed mesoporous structure with the large pores, which provided high surface area and accessibility to the active sites, made the catalyst exhibit outstanding performance both in the half-cell and single-cell systems. These two main factors for the high-performance fuel cell cathode catalyst were combined effectively in a simple soft-template synthesis assisted by block co-polymer self-assembly. It is truly noteworthy that an Fe/N/C catalyst with ordered mesoporous structure and Fe-N_x/C molecule-type active sites was synthesized by a new and simple method, and that the advantages of mesoporous structure with an appropriate pore size in metal-containing NPMCs were elucidated.
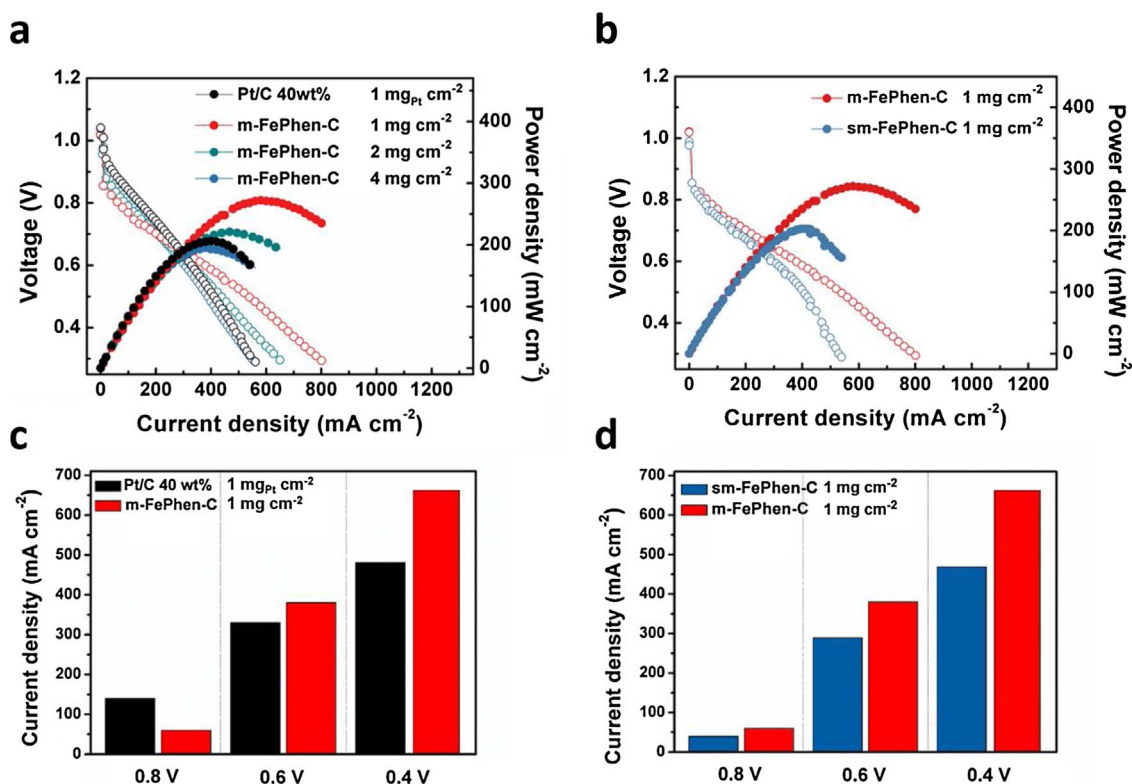
Fig. 6. (a, b) Single-cell performance of AEMFCs with m-FePhen-C, Pt/C (40 wt.%), and sm-FePhen-C cathode catalysts. The catalyst loading amount of m-FePhen-C was changed from 1 to 4 mg cm^{-2}. (c, d) Current densities at the potentials where reaction kinetics (0.8 V), ohmic resistance (0.6 V), and mass transport (0.4 V) are the dominant factors for voltage loss.

Acknowledgements

Appendix A. Supplementary data

Supplementary data associated with this article can be found, in the online version, at http://dx.doi.org/10.1016/j.apcatb.2017.10.015.

References

[1] H.A. Gasteiger, S.S. Kocha, B. Sompalli, F.T. Wagner, Activity benchmarks and requirements for Pt, Pt-alloy, and non-Pt oxygen reduction catalysts for PEMFCs, Appl. Catal. B 56 (2005) 9–35.

[2] D.-W. Wang, D. Su, Heterogeneous nanocarbon materials for oxygen reduction reaction, Energy Environ. Sci. 7 (2014) 576–591.

[3] N. Ranjbar Sahraie, J.P. Paraknowitsch, C. Göbel, A. Thomas, P. Strasser, Noble-metal-free electrocatalysts with enhanced ORR performance by task-specific functionalization of carbon using ionic liquid precursor systems, J. Am. Chem. Soc. 136 (2014) 14486–14497.

[4] J. Greeley, I.E.L. Stephens, A.S. Bondarenko, T.P. Johansson, H.A. Hansen, T.F. Jaramillo, J. Rossmeisl, I. Chorkendorff, J.K. Nørskov, Alloys of platinum and early transition metals as oxygen reduction electrocatalysts, Nat. Chem. 1 (2009) 552–556.

[5] D. Wang, H.L. Xin, R. Hovden, H. Wang, Y. Yu, D.A. Muller, F.J. DiSalvo, H.D. Abruña, Structurally ordered intermetallic platinum-cobalt core-shell nanoparticles with enhanced activity and stability as oxygen reduction electrocatalysts, Nat. Mater. 12 (2013) 81–87.

[6] V.R. Stamenkovic, B. Fowler, B.S. Mun, G. Wang, P.N. Ross, C.A. Lucas, N.M. Marković, Improved oxygen reduction activity on Pt$_3$Ni(111) via increased surface site availability, Science 315 (2007) 493–497.

[7] E. Proietti, F. Jaouen, M. Lefèvre, N. Larouche, J. Tian, J. Herranz, J.-P. Dodelet, Iron-based cathode catalyst with enhanced power density in polymer electrolyte membrane fuel cells, Nat. Commun. 2 (2011) 416.

[8] G. Wu, K.L. More, C.M. Johnston, P. Zelenay, High-performance electrocatalysts for oxygen reduction derived from polyaniline, iron, and cobalt, Science 332 (2011) 443–447.

[9] F. Jaouen, E. Proietti, M. Lefevre, R. Chenitz, J.-P. Dodelet, G. Wu, H.T. Chung, C.M. Johnston, P. Zelenay, Recent advances in non-precious metal catalysis for oxygen-reduction reaction in polymer electrolyte fuel cells, Energy Environ. Sci. 4 (2011) 114–130.

[10] J. Liang, Y. Jiao, M. Jaroniec, S.Z. Qiao, Sulfur and nitrogen dual-doped mesoporous graphene electrocatalyst for oxygen reduction with synergistically enhanced performance, Angew. Chem. Int. Ed. 51 (2012) 11496–11500.

[11] L. Zhang, Z. Xia, Mechanisms of oxygen reduction reaction on nitrogen-doped graphene for fuel cells, J. Phys. Chem. C 115 (2011) 11170–11176.

[12] K. Gong, F. Du, Z. Xia, M. Durstock, L. Dai, Nitrogen-doped carbon nanotube arrays with high electrocatalytic activity for oxygen reduction, Science 323 (2009) 760–764.

[13] M. Borghei, N. Laocharoen, E. Kibena-Põldsepp, L.-S. Johansson, J. Campbell, E. Kauppinen, K. Tammeveski, O.J. Rojas, Porous N,P-doped carbon from coconut shells with high electrocatalytic activity for oxygen reduction: alternative to Pt-C for alkaline fuel cells, Appl. Catal. B 204 (2017) 394–402.

[14] R. Jasinski, Cobalt phthalocyanine as a fuel cell cathode, J. Electrochem. Soc. 112 (1965) 526–528.

[15] J.Y. Cheon, T. Kim, Y. Choi, H.Y. Jeong, M.G. Kim, Y.J. Sa, J. Kim, Z. Lee, T.-H. Yang, K. Kwon, O. Terasaki, G.-G. Park, R.R. Adzic, S.H. Joo, Ordered mesoporous porphyrinic carbons with very high electrocatalytic activity for the oxygen reduction reaction, Sci. Rep. 3 (2013) 2715–2722.

[16] J. Liang, R.F. Zhou, X.M. Chen, Y.H. Tang, S.Z. Qiao, Fe-N decorated hybrids of CNTs grown on hierarchically porous carbon for high-performance oxygen reduction, Adv. Mater. 26 (2014) 6074–6079.

[17] M. Lefèvre, E. Proietti, F. Jaouen, J.-P. Dodelet, Iron-based catalysts with improved oxygen reduction activity in polymer electrolyte fuel cells, Science 324 (2009) 71–74.

[18] N. Ramaswamy, U. Tylus, Q. Jia, S. Mukerjee, Activity descriptor identification for oxygen reduction on nonprecious electrocatalysts: linking surface science to coordination chemistry, J. Am. Chem. Soc. 135 (2013) 15443–15449.

[19] A. Zitolo, V. Goellner, V. Armel, M.-T. Sougrati, T. Mineva, L. Stievano, E. Fonda, F. Jaouen, Identification of catalytic sites for oxygen reduction in iron- and nitrogen-doped graphene materials, Nat. Mater. 14 (2015) 937–942.

[20] U. Tylus, Q. Jia, H. Hafiz, R.J. Allen, B. Barbiellini, A. Bansil, S. Mukerjee, Engendering anion immunity in oxygen consuming cathodes based on Fe-N$_x$ electrocatalysts: spectroscopic and electrochemical advanced characterizations, Appl. Catal. B 198 (2016) 318–324.

[21] C. Tang, Q. Zhang, Can metal-nitrogen-carbon catalysts satisfy oxygen electrochemistry? J. Mater. Chem. A 4 (2016) 4998–5001.

[22] U. Tylus, Q. Jia, K. Strickland, N. Ramaswamy, A. Serov, P. Atanassov, S. Mukerjee, Elucidating oxygen reduction active sites in pyrolyzed metal-nitrogen coordinated non-precious-metal electrocatalyst systems, J. Phys. Chem. C 118 (2014) 8999–9008.

[23] Y.J. Sa, D.-J. Seo, J. Woo, J.T. Lim, J.Y. Cheon, S.Y. Yang, J.M. Lee, D. Kang,

T.J. Shin, H.S. Shin, H.Y. Jeong, C.S. Kim, M.G. Kim, T.-Y. Kim, S.H. Joo, A general approach to preferential formation of active Fe-N$_x$ sites in Fe-N/C electrocatalysts for efficient oxygen reduction reaction, J. Am. Chem. Soc. 138 (2016) 15046–15056.

[24] Y. Zhu, B. Zhang, X. Liu, D.-W. Wang, D.S. Su, Unravelling the structure of electrocatalytically active Fe-N complexes in carbon for the oxygen reduction reaction, Angew. Chem. Int. Ed. 53 (2014) 10673–10677.

[25] J. Sanetuntikul, S. Shanmugam, High pressure pyrolyzed non-precious metal oxygen reduction catalysts for alkaline polymer electrolyte membrane fuel cells, Nanoscale 7 (2015) 7644–7650.

[26] T.J. Schmidt, H.A. Gasteiger, G.D. Stäb, P.M. Urban, D.M. Kolb, R.J. Behm, Characterization of high-surface-area electrocatalysts using a rotating disk electrode configuration, J. Electrochem. Soc. 145 (1998) 2354–2358.

[27] M.K. Debe, Electrocatalyst approaches and challenges for automotive fuel cells, Nature 486 (2012) 43–51.

[28] S. Lee, M. Choun, Y. Ye, J. Lee, Y. Mun, E. Kang, J. Hwang, Y.-H. Lee, C.-H. Shin, S.-H. Moon, S.-K. Kim, E. Lee, J. Lee, Designing a highly active metal-free oxygen reduction catalyst in membrane electrode assemblies for alkaline fuel cells: effects of pore size and doping-site position, Angew. Chem. Int. Ed. 54 (2015) 9230–9234.

[29] L. Gu, L. Jiang, X. Li, J. Jin, J. Wang, G. Sun, A Fe-N-C catalyst with highly dispersed iron in carbon for oxygen reduction reaction and its application in direct methanol fuel cells, Chin. J. Catal. 37 (2016) 539–548.

[30] S. Zhao, H. Yin, L. Du, L. He, K. Zhao, L. Chang, G. Yin, H. Zhao, S. Liu, Z. Tang, Carbonized nanoscale metal-organic frameworks as high performance electrocatalyst for oxygen reduction reaction, ACS Nano 8 (2014) 12660–12668.

[31] R. Janarthanan, A. Serov, S.K. Pilli, D.A. Gamarra, P. Atanassov, M.R. Hibbs, A.M. Herring, Direct methanol anion exchange membrane fuel cell with a non-platinum group metal cathode based on iron-aminoantipyrine catalyst, Electrochim. Acta 175 (2015) 202–208.

[32] K.K.R. Datta, B.V.S. Reddy, K. Ariga, A. Vinu, Gold nanoparticles embedded in a mesoporous carbon nitride stabilizer for highly efficient three-component coupling reaction, Angew. Chem. Int. Ed. 49 (2010) 5961–5965.

[33] J. Rosen, G.S. Hutchings, F. Jiao, Ordered mesoporous cobalt oxide as highly efficient oxygen evolution catalyst, J. Am. Chem. Soc. 135 (2013) 4516–4521.

[34] C. Chen, J. Kim, W.-S. Ahn, CO$_2$ capture by amine-functionalized nanoporous materials: a review, Korean J. Chem. Eng. 31 (2014) 1919–1934.

[35] J.K. Dombrovskis, H.Y. Jeong, K. Fossum, O. Terasaki, A.E.C. Palmqvist, Transition metal ion-chelating ordered mesoporous carbons as noble metal-free fuel cell catalysts, Chem. Mater. 25 (2013) 856–861.

[36] J. Lee, S. Yoon, T. Hyeon, S.M. Oh, K.B. Kim, Synthesis of a new mesoporous carbon and its application to electrochemical double-layer capacitors, Chem. Commun. (1999) 2177–2178.

[37] C. Jo, I. Hwang, J. Lee, C.W. Lee, S. Yoon, Investigation of pseudocapacitive charge-storage behavior in highly conductive ordered mesoporous tungsten oxide electrodes, J. Phys. Chem. C 115 (2011) 11880–11886.

[38] S. Jun, S.H. Joo, R. Ryoo, M. Kruk, M. Jaroniec, Z. Liu, T. Ohsuna, O. Terasaki, Synthesis of new, nanoporous carbon with hexagonally ordered mesostructure, J. Am. Chem. Soc. 122 (2000) 10712–10713.

[39] B.T. Yonemoto, G.S. Hutchings, F. Jiao, A general synthetic approach for ordered mesoporous metal sulfides, J. Am. Chem. Soc. 136 (2014) 8895–8898.

[40] P. Kim, J.B. Joo, J. Kim, W. Kim, I.K. Song, J. Yi, Sucrose-derived graphitic porous carbon replicated by mesoporous silica, Korean J. Chem. Eng. 23 (2006) 1063–1066.

[41] J. Hwang, C. Jo, K. Hur, J. Lim, S. Kim, J. Lee, Direct access to hierarchically porous inorganic oxide materials with three-dimensionally interconnected networks, J. Am. Chem. Soc. 136 (2014) 16066–16072.

[42] R. Liu, Y. Shi, Y. Wan, Y. Meng, F. Zhang, D. Gu, Z. Chen, B. Tu, D. Zhao, Triconstituent co-assembly to ordered mesostructured polymer-silica and carbon-silica nanocomposites and large-pore mesoporous carbons with high surface areas, J. Am. Chem. Soc. 128 (2006) 11652–11662.

[43] J. Lee, M.C. Orilall, S.C. Warren, M. Kamperman, F.J. DiSalvo, U. Wiesner, Direct access to thermally stable and highly crystalline mesoporous transition-metal oxides with uniform pores, Nat. Mater. 7 (2008) 222–228.

[44] Y. Meng, D. Gu, F. Zhang, Y. Shi, H. Yang, Z. Li, C. Yu, B. Tu, D. Zhao, Ordered mesoporous polymers and homologous carbon frameworks: amphiphilic surfactant templating and direct transformation, Angew. Chem. Int. Ed. 44 (2005) 7053–7059.

[45] T.-H. Ko, W.-S. Kuo, Y.-H. Chang, Raman study of the microstructure changes of phenolic resin during pyrolysis, Polym. Compos. 21 (2000) 745–750.

[46] J. Herranz, F. Jaouen, M. Lefèvre, U.I. Kramm, E. Proietti, J.-P. Dodelet, P. Bogdanoff, S. Fiechter, I. Abs-Wurmbach, P. Bertrand, T.M. Arruda, S. Mukerjee, Unveiling N-protonation and anion-binding effects on Fe/N/C catalysts for O$_2$ reduction in proton-exchange-membrane fuel cells, J. Phys. Chem. C 115 (2011) 16087–16097.

[47] S.C. Warren, F.J. DiSalvo, U. Wiesner, Nanoparticle-tuned assembly and disassembly of mesostructured silica hybrids, Nat. Mater. 6 (2007) 156–161.

[48] S.S. Soni, G. Brotons, M. Bellour, T. Narayanan, A. Gibaud, Quantitative SAXS analysis of the P123/water/ethanol ternary phase diagram, J. Phys. Chem. B 110 (2006) 15157–15165.

[49] C. Cartier, M. Momenteau, E. Dartyge, A. Fontaine, G. Tourillon, A. Michalowicz, M. Verdaguer, X-Ray absorption spectroscopy of iron-(II) and -(III) basket-handle porphyrins, J. Chem. Soc. Dalton Trans. (1992) 609–618.

[50] U.I. Kramm, J. Herranz, N. Larouche, T.M. Arruda, M. Lefèvre, F. Jaouen, P. Bogdanoff, S. Fiechter, I. Abs-Wurmbach, S. Mukerjee, J.-P. Dodelet, Structure of the catalytic sites in Fe/N/C-catalysts for O$_2$-reduction in PEM fuel cells, Phys. Chem. Chem. Phys. 14 (2012) 11673–11688.

[51] S.-H. Liu, J.-R. Wu, Influence of nitrogen and iron precursors on the synthesis of FeN$_x$/carbons electrocatalysts toward oxygen reduction reaction in acid solution, Electrochim. Acta 135 (2014) 147–153.

[52] T.-N. Tran, M.Y. Song, K.P. Singh, D.-S. Yang, J.-S. Yu, Iron-polypyrrole electrocatalyst with remarkable activity and stability for ORR in both alkaline and acidic conditions: a comprehensive assessment of catalyst preparation sequence, J. Mater. Chem. A 4 (2016) 8645–8657.

[53] D. Long, W. Li, L. Ling, J. Miyawaki, I. Mochida, S.-H. Yoon, Preparation of nitrogen-doped graphene sheets by a combined chemical and hydrothermal reduction of graphene oxide, Langmuir 26 (2010) 16096–16102.

[54] B. Jeong, D. Shin, H. Jeon, J.D. Ocon, B.S. Mun, J. Baik, H.-J. Shin, J. Lee, Excavated Fe-N-C sites for enhanced electrocatalytic activity in the oxygen reduction reaction, ChemSusChem 7 (2014) 1289–1294.

[55] Y. Wang, Y. Nie, W. Ding, S.G. Chen, K. Xiong, X.Q. Qi, Y. Zhang, J. Wang, Z.D. Wei, Unification of catalytic oxygen reduction and hydrogen evolution reactions: highly dispersive Co nanoparticles encapsulated inside Co and nitrogen co-doped carbon, Chem. Commun. 51 (2015) 8942–8945.

[56] X. Li, H. Wang, J.T. Robinson, H. Sanchez, G. Diankov, H. Dai, Simultaneous nitrogen doping and reduction of graphene oxide, J. Am. Chem. Soc. 131 (2009) 15939–15944.

[57] S. Mutyala, J. Mathiyarasu, A. Mulchandani, Methanol tolerant high performance, noble metal free electrocatalyst developed from polyaniline and ferric chloride for the oxygen reduction reaction, RSC Adv. 5 (2015) 92648–92655.

[58] S. Liu, C. Deng, L. Yao, H. Zhong, H. Zhang, The key role of metal dopants in nitrogen-doped carbon xerogel for oxygen reduction reaction, J. Power Sources 269 (2014) 225–235.

[59] J. Sanetuntikul, C. Chuaicham, Y.-W. Choi, S. Shanmugam, Investigation of hollow nitrogen-doped carbon spheres as non-precious Fe-N$_4$ based oxygen reduction catalysts, J. Mater. Chem. A 3 (2015) 15473–15481.

[60] T.-H. Ko, W.-S. Kuo, Y.-H. Chang, Microstructural changes of phenolic resin during pyrolysis, J. Appl. Polym. Sci. 81 (2001) 1084–1089.

[61] A.L. Evelyn, D. Ila, G.M. Jenkins, RBS and Raman spectroscopy study of heat-treatment effect on phenolformaldehyde resin, Nucl. Instrum. Methods Phys. Res. B 85 (1994) 861–863.

[62] F. Jaouen, F. Charreteur, J.P. Dodelet, Fe-Based catalysts for oxygen reduction in PEMFCs: importance of the disordered phase of the carbon support, J. Electrochem. Soc. 153 (2006) A689–A698.

[63] M.S. Thorum, J.M. Hankett, A.A. Gewirth, Poisoning the oxygen reduction reaction on carbon-supported Fe and Cu electrocatalysts: evidence for metal-centered activity, J. Phys. Chem. Lett. 2 (2011) 295–298.

[64] Y. Tang, J. Zhang, C. Song, H. Liu, J. Zhang, J. Zhang, H. Wang, S. Mackinnon, T. Peckham, J. Li, S. McDermid, P. Kozak, Temperature dependent performance and in situ AC impedance of high-temperature PEM fuel cells using the Nafion-112 membrane, J. Electrochem. Soc. 153 (2006) A2036–A2043.

[65] T.V. Reshetenko, H.-T. Kim, H.-J. Kweon, Modification of cathode structure by introduction of CNT for air-breathing DMFC, Electrochim. Acta 53 (2008) 3043–3049.

[66] Y.-H. Cho, J.W. Lim, Y.S. Kang, Y.-H. Cho, O.-H. Kim, N.-H. Kwon, O.J. Kwon, W.-S. Yoon, H. Choe, Y.-E. Sung, The dependence of performance degradation of membrane electrode assembly on platinum loading in polymer electrolyte membrane fuel cell, Int. J. Hydrogen Energy 37 (2012) 2490–2497.

[67] Y.-H. Cho, N. Jung, Y.S. Kang, D.Y. Chung, J.W. Lim, H. Choe, Y.-H. Cho, Y.-E. Sung, Improved mass transfer using a pore former in cathode catalyst layer in the direct methanol fuel cell, Int. J. Hydrogen Energy 37 (2012) 11969–11974.

[68] Y.G. Yoon, G.G. Park, T.H. Yang, J.N. Han, W.Y. Lee, C.S. Kim, Effect of pore structure of catalyst layer in a PEMFC on its performance, Int. J. Hydrogen Energy 28 (2003) 657–662.

[69] E. Passalacqua, F. Lufrano, G. Squadrito, A. Patti, L. Giorgi, Influence of the structure in low-Pt loading electrodes for polymer electrolyte fuel cells, Electrochim. Acta 43 (1998) 3665–3673.

[70] S. Gamburzev, A.J. Appleby, Recent progress in performance improvement of the proton exchange membrane fuel cell (PEMFC), J. Power Sources 107 (2002) 5–12.